promoting access to White Rose research papers

Universities of Leeds, Sheffield and York
http://eprints.whiterose.ac.uk/

This is an author produced version of a paper published in **Geophysical Journal International**
White Rose Research Online URL for this paper:

http://eprints.whiterose.ac.uk/id/eprint/77385

Paper:
Hammond, JOS, Kendall, J-M, Angus, DAC and Wookey, J (2010) *Interpreting spatial variations in anisotropy: insights into the Main Ethiopian Rift from SKS waveform modelling.* Geophysical Journal International, 181 (3). 1701 - 1712.
ISSN 0956-540X
http://dx.doi.org/10.1111/j.1365-246X.2010.04587.x

White Rose Research Online
eprints@whiterose.ac.uk

submitted to *Geophys. J. Int.*

Interpreting spatial variations in anisotropy: Insights into the Main Ethiopian Rift from SKS waveform modelling

J. O. S. Hammond[1], J-M. Kendall[1], D. Angus[1,2], and J. Wookey[1]

[1]*Department of Earth Sciences, University of Bristol, Wills Memorial Building, Queens Road, Bristol, BS8 1RJ, UK*

[2]*School of Earth and Environment, University of Leeds, Leeds, LS2 9JT, UK*

3 March 2010

SUMMARY

Seismic anisotropy is a common feature in the upper mantle and measuring shear-wave splitting in core phases is a common approach in estimating its characteristics. Large lateral variations in estimated splitting parameters are observed over small spatial distances in many differing tectonic regions, including areas of continental break-up such as the Main Ethiopian Rift (MER). We investigate the ability of shear-wave splitting analysis to constrain spatial variations in anisotropy using a one-way wave equation modelling scheme to generate band-limited waveforms for a suite of models representing regions with rapidly changing anisotropy. We show that shear-wave splitting can identify lateral variation in anisotropy on the order of 20-50 km, where a change in fast direction demarcates the transition in anisotropy. Additionally, variation in the amount of splitting is complicated close to the transition, and is sensitive to the vertical thickness of anisotropy. We have used these modelling results to interpret shear-wave splitting measurements for the Main Ethiopian Rift. The model that best fits the observations has a 100 km wide rift zone with a fast direction of 30° outside and 20° inside the rift. The model has 9% anisotropy close to the western margin, with 7% anisotropy elsewhere. In all regions of the model we constrain the anisotropy to begin at a depth of 90 km. The depth of anisotropy is consistent with geochemical estimates of the depth of melt initiation beneath the region. Also the elevated splitting beneath the western margin supports evidence of low velocities and highly conductive zones from seismic tomography and magneto-tellurics, suggesting melt is more focused along the western margin. This study shows how observations of *SKS*-wave splitting from dense seismic networks can be used to map sharp lateral changes and constrain the depth of the anisotropy.

Key words:

1 INTRODUCTION

Seismic anisotropy can be described as the variation of seismic wave speed with direction of propagation. In most studies the main cause of anisotropy in the upper mantle is assumed to be the lattice preferred orientation (LPO) of olivine where the olivine fast axis (a-axis) aligns in the direction of upper-mantle flow (Babuska & Cara, 1991; Mainprice et al., 2000). This could be caused by current mantle processes, or due to accumulated strain which has 'frozen' in an anisotropic signature from previous deformation events. Other mechanisms that cause upper mantle anisotropy are fluid filled cracks (Crampin & Booth, 1985) or the preferred orientation of inclusions (e.g., oriented melt pockets (OMP), see Kendall, 1994; Blackman & Kendall, 1997) mechanisms that can be very efficient at generating large amounts of anisotropy (Kendall, 2000).

A common way of constraining anisotropy in the upper mantle is shear-wave splitting analysis. When a shear-wave enters an anisotropic medium it splits into two quasi-shear waves that are polarised orthogonally to each other and propagate with different velocities. These split shear-waves can be used to characterise anisotropy in terms of an apparent symmetry axis (typically fast shear-wave direction, ϕ) and the time-lag between fast and slow shear waves (δt, a proxy for amount, or extent of anisotropy).

Many studies investigating upper mantle anisotropy based on shear-wave splitting utilise *SKS*-phases. This is a wave that travels as an *S*-wave through the mantle and a *P*-wave through the outer core. It is advantageous to use this phase because it is a clear arrival over a range of epicentral distances (85°-120°), making it observable in most regions. Also, it is possible to ignore source side anisotropy due to the fact that the seismic energy converts to a *P*-wave at the CMB, thus the measured anisotropy can be attributed to the mantle beneath the station. Another benefit is that the rays travel almost vertically in the uppermost mantle making *SKS*-wave splitting a useful tool to distinguish lateral variations in anisotropy (see Silver, 1996; Savage, 1999; Kendall, 2000, for examples). However, due to the near vertical raypaths it is very hard to place any constraints on the depth extent of anisotropy, which has led to much debate on whether anisotropy can be attributed to lithospheric fabric (fossil anisotropy (Silver, 1996), fluid filled cracks (Crampin & Booth, 1985)), or asthenospheric processes (for example, flow at plate boundaries (Blackman & Kendall, 2002), simple asthenospheric flow (Savage, 1999), density driven flow (Behn et al., 2004)).

Some attempt has been made to constrain the depth extent of anisotropy based on consideration of *SKS* Fresnel zones (Alsina & Snieder, 1995; Rümpker & Ryberg, 2000). For instance, it can be assumed that two different splitting results from nearby stations indicate that the *SKS*-waves are sampling different anisotropic regions. Thus, the depth of origin of the anisotropy can be estimated as anywhere shallower than the depth where the Fresnel zones beneath each station overlap. Favier & Chevrot (2003) and Chevrot et al. (2004) apply a finite-frequency Frechet derivative approach and calculate 3-D sensitivity kernels for shear-wave splitting intensity, which are similar to those estimated from Fresnel zone estimates (Alsina & Snieder, 1995; Rümpker & Ryberg, 2000).

Other studies have utilised finite difference modelling schemes to investigate the ability of shear-wave splitting to identify lateral and depth variations in anisotropy (e.g., Rümpker & Silver, 2000), and have placed some constraints on the distribution of anisotropy beneath transform faults and shear zones **(Rümpker et al., 2003; Chevrot, 2006; Chevrot & Monteiller, 2009)** and a plume setting (Rümpker & Silver, 2000). All these studies show that regions with laterally varying anisotropy give rise to complicated splitting measurements.

In this paper we address the suitability of the *SKS*-wave splitting technique to constrain sharp lateral variations in anisotropy, and further investigate the ability of this seismological technique to constrain the depth extent of the anisotropy. This is done using a finite-frequency waveform modelling technique (Angus et al., 2004). This study improves on previous modeling of laterally varying anisotropy by providing some general guidelines that can be applied to shear-wave splitting observations in regions with sharp lateral changes in anisotropy. This study was motivated by observations of *SKS*-wave splitting beneath the Main Ethiopian Rift (MER) (Kendall et al., 2005, 2006), and these results are used as a case study to highlight the utility of the modeling. This approach is applicable to any region that has sharp boundaries in anisotropy, such as transform faults or suture zones.

2 FINITE FREQUENCY WAVEFORM MODELLING

We construct synthetic seismograms using the one-way wave equation modelling scheme of Angus et al. (2004) and Angus & Thomson (2006), for waves propagating vertically through a medium containing oriented melt pockets (Figure 2). The model is constructed by calculating the elastic constants for vertically aligned melt pockets, using the approach of Hudson (1981) and applying these elastic constants at each node. The elastic constants are calculated using *P*- and *S*-wave velocities of 7.8 kms^{-1} and 4.0 kms^{-1} (matrix material) and 2.5 kms^{-1} and 0.0 kms^{-1} (crack material) and densities of 3.8 $\mathrm{kg/m}^3$ and 2.7 $\mathrm{kg/m}^3$ for the matrix material and crack material, respectively. The cracks consist of penny shaped inclusions with an aspect ratio of 0.01. Crack density is then varied to calculate elastic constants with varying magnitudes of anisotropy. We characterise this anisotropy in terms of maximum shear-wave anisotropy (i.e. 10% anisotropy refers to a maximum shear-wave anisotropy of 10%). Motivated by Kendall et al. (2005) a MER rift-like model is constructed (Figure 2) (e.g., a rotated horizontal symmetry axis in the rift zone). The simulations are done in 3D, but with only 2D variations in anisotropy.

In the models the fast direction is oriented 30° from north outside the rift, and north-south inside the rift. An *SKS* like wave (i.e. small waveform curvature (4.2^{-12} s/m), 8 s period) is then propagated through the 3D anisotropic model using the finite-difference one-way wave propagator formulation (Angus et al., 2004; Angus & Thomson, 2006). There is a sharp transition between these two regions (i.e. grid points on either side of the transition between rift and flank have differing fast axis orientations and hence elastic constants). The one-way wave equation method models transmitted waves (it ignores backscattering which is not an issue in modelling *SKS*-wave arrivals), taking into account frequency dependent coupling effects due to, for instance, rapidly rotating wave polarisation effects due to slowness surfaces (Crampin & Yedlin, 1981).

Model number	Varying parameter	Range	Figure
1	Width of anisotropic zone	5-40 km	1
2	Magnitude of anisotropy	4-10%	2
3	Depth extent of anisotropy	25-85 km	3
4	Dominant period of incoming wave	0.5-10 s	4
5	Initial polarisation of incoming wave	15-165°	5

Table 1. Parameters tested in the various models

All waves are **Ricker wavelets (although wavelet type has no effect on the result)**, have a dominant period of 8 s (except model 6, where frequency dependence is investigated), and initial source polarisation of 45° (except model 7, where initial polarisation dependence is investigated). The output waveforms are then analysed identically to the data (see Kendall et al., 2005), and the apparent splitting is estimated for a profile spanning the 'rift' zone. **To estimate the splitting we use the Teanby et al. (2004) cluster analysis method which is based on the Silver & Chan (1991) method. This technique performs a grid search over δt and ϕ, rotating the horizontal components by ϕ, and shifting their relative positions by δt. The values of δt and ϕ which provide the most linear particle motion provides our estimate of the splitting. A statistical F-test is used to asses the uniqueness of the result, thus providing an error estimate.** The observed splitting depends on several parameters (outlined in Table 1) and each parameter is studied in turn (Figures 3-7). Finally, based on the modelling results, the observed splitting parameters of Kendall et al. (2005) (Figure 1) are modelled to place estimates on the anisotropic characteristics beneath the MER.

2.1 Model class 1: Varying width of 'rift' zone

The first variable tested is rift width (all other variables are held constant: maximum *S*-wave anisotropy=10%, depth of anisotropy=45 km (from surface), dominant period=8 s, initial polarisation=45°). We vary the width of the rift zone between 100 km and **10 km** (Figure 3). A smooth transition in ϕ is seen for all rift widths. The inflexion point in the ϕ profile marks the boundary between anisotropic regions (Figure 3). However, δt shows considerably more variation across the rift boundaries. The expected δt for this model is a constant value of 1.27 s, but we see large variations, similar to those seen for other studies of inhomogeneous anisotropic media (e.g., plume, Rümpker & Silver (2000); transform fault, Rümpker et al. (2003)).

2.2 Model class 2: Varying magnitude of anisotropy

The second variable tested is the magnitude of anisotropy (all other parameters are held constant: rift width=40 km, depth of anisotropy=45 km (from surface), dominant period=8 s, initial polarisation=45°). All models within this class show a smooth transition in ϕ, with the inflexion point showing the transition between anisotropic regions. The δt profile shows a similar trend for all models. The magnitude of splitting depends on the amount of anisotropy, but the peaks and troughs of the δt curve all lie in the same place (see Figure 4).

2.3 Model class 3: Varying thickness of anisotropic zone

The third variable tested is depth (i.e. thickness from the surface) of the anisotropic zone (all other parameters are held constant: rift width=40 km, maximum *S*-wave anisotropy=10%, dominant period=8 s, initial polarisation=45°). The variation of ϕ is smooth for nearly all models in this class, with the inflexion point showing the transition between anisotropic regions. An exception occurs in the model with an 85 km thick layer (Figure 5). The variation in ϕ seen in the 85 km thick layer has some deviation at the boundary between anisotropic regions. This may be due to multipathing effects; a result of the longer wavepath through a complex, highly anisotropic medium. The δt curve shows similar variation to that seen in model 2. Although similar to model 2, where the magnitude of splitting increases with anisotropic strength rather than increasing path length, there is an observable moveout of the peaks with increasing thickness (Figure 5). This sensitivity with depth can be used to interpret something about the depth to the anisotropic region. We discuss this further in relation to the MER results in section 3.1.

2.4 Model class 4: Varying frequency of propagating wave

The fourth variable tested is the dominant period of the incoming wave (all other parameters are held constant: rift width=40 km, maximum *S*-wave anisotropy=10%, depth of anisotropy=45 km, initial polarisation=45°). It is evident that varying the dominant period has a large effect on the variation observed in both δt and ϕ (Figure 6). For higher frequencies the curves match the input model well, with little deviation in δt and a sharp transition in ϕ. The observation that the inflexion points in ϕ describe the width of the rift zone still applies for all frequencies. For higher frequencies the peaks in δt are narrow, an effect of approaching the ray theoretical limit. This shows the importance of investigating shear-wave splitting using a finite-frequency approach, where the influence of frequency dependent shear-wave coupling is accounted for.

2.5 Model class 5: Varying initial polarisation of the incoming shear wave

The fifth variable tested is the initial polarisation of the incoming wave (all other parameters are held constant: rift width=40 km, maximum *S*-wave anisotropy=10%, depth of anisotropy=45 km, dominant period=8 s). The variation in ϕ is dependent on the initial polarisation, but the inflexion points still define the width of the rift zone (Figure 7). The transition in ϕ from 30° to 0° occurs over distances of $\sim$20-50 km. It is evident that δt is strongly dependent on the initial polarisation, with the peaks in δt occurring either side, and on top of the transition between anisotropic regions (Figure 7). This is similar to previous studies of inhomogeneous anisotropic structure which show that the measured splitting parameters are highly dependent on the initial polarisation of the shear-wave (Silver & Savage, 1994; Rümpker & Silver, 2000; Rümpker et al., 2003).

The variation in the δt profile depends on the relationship between the initial polarisation and the two anisotropic symmetry axes. For example, model 5 shows that for an initial polarisation of 105° the peak in the δt curve lies directly above the transition zone. This initial polarisation is oriented 75° from both the 30° fast direction outside the rift, and the 0° inside the rift (105° = -75°). **However, when the initial polarisation is preferentially close to one of the symmetry axis (assuming it is not so close that a null measurement is recorded), it will induce an asymmetry in the observed δt measurements.** This result is consistent with the observation that the finite-frequency sensitivity kernel of the incoming shear-wave depends on the initial polarisation (Favier & Chevrot, 2003; Chevrot et al., 2004).”

3 DISCUSSION

For all the scenarios modelled in section 2 it is evident that sharp lateral changes in anisotropic fabric can be detected using shear-wave splitting. The sharpness of the transition in splitting parameters depends on three parameters, the thickness of the anisotropic layer (Figure 5), the frequency of the incoming wave (Figure 6) and the initial polarisation of the shear-wave (Figure 7). For example, for an 8 s wave (e.g., *SKS*), the transition in ϕ from 30° to 0° occurs over $\sim$20 km (25 km thick layer) to $\sim$40 km (85 km thick layer), assuming a constant initial polarisation. For a constant thickness of anisotropy (45 km) the transition in ϕ varies from $\sim$20-50 km, depending on the initial polarisation. In all model classes, except where the splitting is very large, the inflexion points in the ϕ curve define the transition in anisotropic fabric. For the MER this will indicate the rift width, but this phenomenon can also potentially be used to determine the location of transform faults and suture zones.

Having constrained the rift width from ϕ it is possible to use the variation in δt to place constraints on the thickness of the anisotropic layer. The position of the peaks and troughs in δt vary for differing rift widths, frequency content of the incoming wave, thickness of the anisotropic layer and initial polarisation. By assuming a dominant period of the incoming *SKS*-phase of 8 s, we can use the position of the peaks and troughs to estimate the thickness of the anisotropic layer. This can only be done for one initial polarisation (approximately the same as back-azimuth for an *SKS*-wave).

From studying the variations in ϕ and δt we can estimate the width and thickness of the anomalous anisotropic zone, and from this it is simple to estimate the magnitude of anisotropy. The magnitude of anisotropy is calculated by determining the amount needed to match the splitting results far from the rift. In our models we impose a vertical transition in anisotropic regions. We acknowledge that dipping boundaries may effect these results, and more modeling is need to constrain this.

This modeling exercise has highlighted other features which may be observable in data to detect lateral variations in anisotropy. It is evident that stations close to the transition will show large variation in δt as a function of back-azimuth, whereas the same stations will show little variation of ϕ. This is notably different from what is expected from two horizontal layers of splitting, which causes variations in both ϕ and δt (Silver & Savage, 1994). Another feature which can be observed is the variation of δt as a function of frequency, again close to the transition in anisotropic domains.

3.1 Comparison with the Main Ethiopian Rift (MER)

Kendall et al. (2005) observe a rotation in the splitting fast direction inside the Main Ethiopian rift valley, with the fast shear-wave aligning with the magmatic segments (Figure 1). This pattern could be caused by oriented melt pockets (OMP) or along-rift flow which causes a lattice preferred orientation (LPO) of olivine. A study of surface waves **(Kendall et al., 2006; Bastow et al., in review 2010)** addresses this ambiguity, due to the azimuthal variations expected for observed phase velocities on interstation paths being different for OMP or LPO. **Kendall et al. (2006) and Bastow et al. (in review 2010)** show that to satisfy both the *SKS*-wave splitting results and surface wave results an OMP source of anisotropy, down to depths of at least 70 km, must be present. Keir et al. (2005) analysed splitting in shear-waves from local earthquakes $<$20 km beneath the MER, and found fast directions similar to Kendall et al. (2005), aligning with the magmatic segments. They also found elevated splitting magnitudes above regions where melt has been inferred from wide-angle refraction (Mackenzie et al., 2005) and controlled source tomography (Keranen et al., 2004).

Other *SKS*-wave splitting results around Ethiopia show similar results. Ayele et al. (2004) observed splitting in Kenya, Ethiopia and Djibouti, and noticed that the magnitude of splitting increases with the amount of melt produced, inferred from a correlation between an increase in delay time and volcanism. Gashawbeza et al. (2004) performed shear-wave splitting on a network of wider aperture, but similar location to Kendall et al. (2005). They observed similar rift parallel trends in the fast directions, but argued that fossilised Precambrian anisotropy was the source of this splitting, with some more recent Neogene influence near the rift to explain the rotation in the fast directions.

Melt has been observed beneath the plateau in the form of highly conductive bodies in magneto-telluric surveys (Whaler & Hautot, 2006), and underplating is observed in wide-angle reflection profiles (Mackenzie et al., 2005). It seems likely that a combination of both pre-existing fabric, and melt induced anisotropy could be present beneath the plateau region. Further evidence of melt beneath the MER comes from receiver function studies. High values of Poisson's ratio >0.3 for the average crust, and underplating highlight the likelihood of melt beneath Afar (Dugda & Nyblade, 2006) and the MER (Stuart et al., 2006).

Using the criteria outlined in the previous section we can match the pattern of results observed by Kendall et al. (2005) (Figure 1), and thus place more constraints on melt induced anisotropy beneath the MER .

As was shown in the previous section, the variation of ϕ is relatively insensitive to all parameters (assuming an instantaneous change in anisotropic parameters at the transition), and the observation that the 'rift' width can be defined by the inflexion points is robust, except in the presence of very high splitting. For the EAGLE dataset, this results in a rift width of $\sim$100 km, based on all the splitting results from different back-azimuths, with a fast direction of 30° outside the rift, and 20° inside the rift (Figure 9).

We have shown that variation in δt is dependent on frequency, initial polarisation and vertical thickness of the anisotropic zone. **To model this event we take a real SKS waveform from the Ethiopian seismic station ADEE (Figure 8) (see Bastow et al., 2008, for station details), and propagate this through the model . However, an 8 s Ricker wavelet, as used in the previous sections, produces identical results.** We can not use all the data, as we did for measuring the rift width, as they come from differing back-azimuths. To account for this we take results from one very well constrained *SKS*-wave splitting event that was recorded across the whole array. This event has a back-azimuth of 40°. We run a model, based on this information, to estimate the depth of the anisotropy. The model has a 100 km wide rift zone, 10% anisotropy, a fast direction of 30° outside the rift and 20° inside, an initial polarisation of 40° and a period of 8 s (Figure 10). It is evident that the peaks are moving out with anisotropic thickness, and if we plot the peak-peak width as a function of depth it is evident that they lie on a straight line (Figure 10). This observation is valid for initial polarisations which fall outside the null planes of either of the anisotropic regions, and outside the null planes for effective splitting parameters observed near the transition between anisotropic regions. For the event with back-azimuth of 40° the peak-peak width is 133 km (Figure 9), which equates to a depth of 90 km. With this information we can estimate the magnitude of anisotropy needed to generate the amount of splitting observed. However, the peaks seen in δt vary in magnitude with the western plateau having elevated shear-wave splitting compared to the eastern plateau. As a result we propose a model which has 9% anisotropy on the western plateau and in the westernmost 30 km of the rift zone and 7% anisotropy on the eastern plateau and easternmost 70 km of the rift zone (Figure 9). **Unfortunately, no other events were suitably recorded across the whole array and thus comparisons of this model with splitting results from other back-azimuths can not be performed.**.

We estimate a region of anisotropy which extends to a depth of ∼90 km beneath the MER, extending beneath the two margins and the rift valley. On the margins the anisotropy is oriented with a fast direction of 30°, and beneath the rift valley the anisotropy is perturbed with an orientation of 20°. The anisotropy below the rift valley correlates with the magmatic segments, as described by Kendall et al. (2005). The variation evident in δt can largely be explained as an effect of these two different anisotropic regimes interacting. The variation in δt is highest on the western margin and results in an estimate of 9% anisotropy beneath this region compared to 7% on the eastern margin. This model is summarised in Figure 11. **This model was estimated using a trial and error approach. To fully constrain this model requires a more complete sampling of the whole model space, which is computationally impractical. As a result we can not formally discuss errors of the fit to the data here. To provide confidence in our models we can compare our results with other geophysical data. To fully explore the model space, studies that invoke theoretical sensitivity kernels may be suitable (Chevrot, 2006; Chevrot & Monteiller, 2009).**

If anisotropy is derived from oriented melt pockets, as suggested by Kendall et al. (2005) then this suggests that melt present beneath the MER is aligned from a depth of 90 km, with an average anisotropy of 7-9%. This equates to a melt fraction of 7-9%, assuming vertically oriented isolated melt inclusions with an aspect ratio of 0.01, but the amount of melt needed to produce this amount of splitting would be smaller for inclusions with a lower aspect ratio.

This estimate of the depth extent of melt induced anisotropy is supported by other studies.

Kendall et al. (2006) show that azimuthal anisotropy seen in surface wave results occurs at depths between 50-70 km, and may extend further but resolution decreases below these depths. Based on simple Fresnel zone estimates, Kendall et al. (2005) place the origin of the anisotropy seen in the EAGLE data to be $<$100 km, a fairly accurate estimate based on these results. *P*- and *S*-wave tomography show the lowest seismic velocities in the top 100 km (Bastow et al., 2005, 2008) (Figure 11) and Ayele et al. (2004) image a discontinuity at a depth of $\sim$90 km which they suggest is the base of the lithosphere. Based on geochemical evidence, Rooney et al. (2005) suggest that the base of the lithosphere is the origin of melt generation feeding the MER. Additionally, Keir et al. (2009) suggest that partial melting of the lithosphere and subsequent magma injection causes lower crustal earthquakes throughout the MER and western plateau.

Seismic tomography (Bastow et al., 2005, 2008) (Figure 11) and magneto-tellurics (Whaler & Hautot, 2006) both show evidence for an asymmetry in melt production, with lower velocities and higher conductivities present beneath the western plateau compared to the eastern plateau. This is supported by our results which show elevated anisotropy in the west, mainly at the region we define as the rift boundary. Holtzman & Kendall (in review) suggest that melt is concentrated in regions of higher strain, and cite the elevated δt seen by Kendall et al. (2005) as evidence for this. We show that an elevated δt can be explained by a simple variation in fast direction alone across the region, but we still require elevated anisotropy close to the western margin, as suggested by Holtzman & Kendall (in review), to explain the asymmetry seen in δt.

4 CONCLUSIONS

We have developed a modelling technique, using a one-way wave equation approach, to investigate the effects of laterally varying anisotropy on shear-wave splitting. We have shown that:

(i) *SKS*-wave splitting can be used to identify changes in fast direction over lateral distances of 20-50 km (dependent on depth and initial polarisation).

(ii) The inflexion points in the ϕ profile demarcate the transition in anisotropy.

(iii) Variation in the position of the peaks and troughs seen in δt depend on anisotropic thickness from the surface, and for a given initial polarisation can be used to place depth constraints on the anisotropic region.

(iv) With information on the depth of the anisotropic region, estimates can be placed on the percentage of anisotropy in the region.

(v) At stations close to the transition δt varies as a function of back-azimuth and frequency, whereas ϕ shows little such variation. This can be used as an indicator of lateral changes in anisotropy

(vi) For higher frequencies the modelled splitting approaches the ray theoretical limit, and shows little variation in δt. Thus, a frequency dependence of δt could indicate a lateral transition in anisotropy. This also shows the importance of performing finite frequency waveform modelling as opposed to ray based approaches in regions where anisotropy varies over length scales comparable to the dominant seismic wavelength.

Determining the exact cause and symmetry of the anisotropy still requires analysis of other phases (e.g., joint shear-wave splitting and surface waves Brisbourne et al. (1999); Kendall et al. (2006)). However, we show that a simple rotation in the anisotropic characteristics in a 100 km wide 'rift' zone can explain much of the variation seen in the Kendall et al. (2005) Main Ethiopian Rift splitting results. The anisotropy across the model is confined to the uppermost 90 km. This region of anisotropy coincides with regions with low velocities (Bastow et al., 2008), high anisotropy (Kendall et al., 2006), high conductivities (Whaler & Hautot, 2006), and the suggested base of the lithosphere (Ayele et al., 2004). It has also been suggested that this region is where melt is generated that feeds the MER (Rooney et al., 2005). However, a simple rotation alone is not enough to reproduce these results. We require elevated anisotropy at the western margin to match the higher δt seen in the splitting results in this region. This coincides with the lowest velocities (Bastow et al., 2008) (Figure 11), highest conductivities (Whaler & Hautot, 2006) and regions of magmatic underplate (Mackenzie et al., 2005; Cornwell et al., 2006). Holtzman & Kendall (in review) suggested that the elevated splitting is caused by focused melt along the margin, where strain is highest. The elevated anisotropy on the western margin required by our models supports this, with little effect seen on the eastern margin where smaller evidence of melt related phenomena are observed. These results show how observations of seismic anisotropy provides insights into the role of magma in rifting.

ACKNOWLEDGMENTS

We thank all involved in the EAGLE project and IRIS for providing the dataset. We also thank Ian Bastow for providing his tomography models, and for useful discussion. Two anonymous reviews are thanked for thoughtful comments which helped improve the paper. This project is funded by NERC (grant no: NE/E005284/1), as part of the Afar Rift Consortium project.

References

Alsina, D. & Snieder, R., 1995. Small-scale sublithospheric continental mantle deformation - constraints form SKS splitting observations, *Geophys. J. Int.*, **123**, 431–448.

Angus, D. A. & Thomson, C. J., 2006. Numerical analysis of a narrow-angle, one-way, elastic-wave equation and extension to curvilinear coordinates, *Geophysics*, **71**(5), 137–146.

Angus, D. A., Thomson, C. J., & Pratt, R. G., 2004. A one-way wave equation for modelling seismic waveform variations due to elastic anisotropy, *Geophys. J. Int.*, **156**, 595–614.

Ayele, A., Stuart, G., & Kendall, J., 2004. Insights into rifting from shear wave splitting and receiver functions: an example from Ethiopia, *Geophysical Journal International*, **157**(1), 354–362.

Babuska, V. & Cara, M., 1991. *Seismic Anisotropy in the Earth*, Kluwer Acad., Norwell, Mass.

Bastow, I., Pilidou, S., Kendall, J.-M., & Stuart, G., in review 2010. Melt-Induced Seismic Anisotropy and Magma Assisted Rifting in Ethiopia: Evidence from Surface Waves.

Bastow, I. D., Stuart, G. W., Kendall, J.-M., & Ebinger, C. J., 2005. Upper-mantle seismic structure in a region of incipient continental breakup: northern Ethiopian rift, *Geophys. J. Int*, **162**, 479–493.

Bastow, I. D., Nyblade, A. A., Stuart, G. W., Rooney, T. O., & Benoit, M. H., 2008. Upper mantle seismic structure beneath the Ethiopian hot spot: Rifting at the edge of the African low-velocity anomaly, *Geochem. Geophys. Geosyst.*, **9**(12), Q12022, doi:10.1029/2008GC002107.

Behn, M. D., Conrad, C. P., & Silver, P. G., 2004. Detection of upper mantle flow associated with the African Superplume, *Earth Planet. Sci. Lett.*, **224**(3–4), 259–274.

Blackman, D. & Kendall, J.-M., 2002. Seismic anisotropy in the upper mantle 2. Predictions for current plate boundary flow models, *Geochem. Geophys. Geosyst.*, **3**(9), 8602.

Blackman, D. K. & Kendall, J.-M., 1997. Sensitivity of teleseismic body waves to mineral texture and melt in the mantle beneath a mid-ocean ridge, *Phil. Trans. R. Soc. Lond. A*, **355**, 217–231.

Brisbourne, A., Stuart, G., & Kendall, J.-M., 1999. Anisotropic structure of the Hikurangi subduction zone, New Zealand-integrated interpretation of surface-wave andbody-wave observations, *Geophys. J. Int.*, **137**(1), 214–230.

Chevrot, S., 2006. Finite-frequency vectorial tomography: a new method for high-resolution imaging of upper mantle anisotropy, *Geophys. J. Int.*, **165**, 641–657.

Chevrot, S. & Monteiller, V., 2009. Principles of vectorial tomography - the effects of model parametrization and regularization in tomographic imaging of seismic anisotropy, *Geophys. J. Int.*, **179**, 1726–1736.

Chevrot, S., Favier, N., & Komatitsch, D., 2004. Shear wave splitting in three-dimensional anisotropic media, *Geophys. J. Int.*, **159**, 711–720.

Cornwell, D. G., Mackenzie, G. D., England, R. W., Maguire, P. K. H., Asfaw, L. M., & Oluma, B., 2006. Northern Main Ethiopian Rift crustal structure from new high-precision gravity data, in *The Afar volcanic province within the east African rift system*, no. 259, pp. 307–321, eds Yirgu, G., Ebinger, C. J., & Maguire, P. K. H., Geological Society, Special Publication, London, UK.

Crampin, S. & Booth, D. C., 1985. Shear-wave polarizations near the North Anatolian Fault, II, Interpretation in terms of crack-induced anisotropy, *Geophys. J. R. Astr. Soc.*, **83**, 75–92.

Crampin, S. & Yedlin, M., 1981. Shear-wave singularities of wave propagation in anisotropic media, *J. Geophys.*, **49**, 43–46.

Dugda, M. T. & Nyblade, A. A., 2006. New constraints on crustal structure in eastern Afar from the analysis of receiver functions and surface wave dispersion in Djibouti, in *The Afar volcanic province within the east African rift system*, no. 259, pp. 55–72, eds Yirgu, G., Ebinger, C. J., & Maguire, P. K. H., Geological Society, Special Publication, London, UK.

Favier, N. & Chevrot, S., 2003. Sensitivity kernels for shear wave splitting in transverse isotropic media, *Geophys. J. Int.*, **153**(1), 213–228.

Gashawbeza, E. M., Klemperer, S. L., Nyblade, A. A., Walker, K. T., & Keranen, K. M., 2004. Shear-wave splitting in Ethiopia: Precambrian mantle anisotropy locally modeified by Neogene rifting, *Geophys. Res. Lett.*, **31**, doi:10.1029/2004GL020471.

Holtzman, B. K. & Kendall, J.-M., in review. Organized melt, seismic anisotropy and plate boundary lubrication, *Geochem. Geophys. Geosyst.*.

Hudson, J., 1981. Wave speeds and attenuation of elastic waves in material containing cracks, *Geophysical Journal International*, **64**(1), 133–150.

Keir, D., Kendall, J.-M., Ebinger, C. J., & Stuart, G. W., 2005. Variations in late syn-rift melt alignment inferred from shear-wave splitting in crustal earthquakes beneath the Ethiopian rift, *Geophys. Res. Lett.*, **32**, doi:10.1029/2005GL024150.

Keir, D., Bastow, I. D., Whaler, K. A., Daly, E., Cornwell, D. G., & Hautot, S., 2009. Lower crustal earthquakes near the Ethiopian rift induced by magmatic processes, *Geochem. Geophys. Geosyst.*, **10**, Q0AB02, doi:10.1029/2009GC002382.

Kendall, J.-M., 1994. Teleseismic arrivals at a mid-ocean ridge: Effects of mantle melt and anisotropy, *Geophys. Res. Lett*, **21**(4), 301–304.

Kendall, J.-M., 2000. Seismic anisotropy in the boundary layers of the mantle, in *Earth's Deep Interior: Mineral Physics and Tomography From the Atomic to the Global Scale*, no. 117, pp. 133–159, eds Karato, S., Forte, A. M., Liebermann, R. C., Masters, G., & Stixrude, L., Geophysical Monograph.

Kendall, J.-M., Stuart, G. W., Ebinger, C. J., Bastow, I. D., & Keir, D., 2005. Magma-assisted rifting in Ethiopia, *Nature*, **433**(7022), 146–148.

Kendall, J.-M., Pilidou, S., Keir, D., Bastow, I. D., Stuart, G. W., & Ayele, A., 2006. Mantle upwellings, melt migration and the rifting of Africa: Insights from seismic anisotropy, in *The*

Afar volcanic province within the east African rift system, no. 259, pp. 55–72, eds Yirgu, G., Ebinger, C. J., & Maguire, P. K. H., Geological Society, Special Publication, London, UK.

Keranen, K., Klemperer, S. L., Gloaguen, R., & Group, E. W., 2004. Three-dimensional seismic imaging of a protoridge axis in the Main Ethiopian rift, *Geology*, **32**(11), 949–952.

Mackenzie, G. D., Thybo, H., & Maguire, P. K. H., 2005. Crustal velocity structure across the Main Ethiopian Rift: results from two-dimensional wide-angle seismic modelling, *Geophys. J. Int.*, **162**(3), 994–1006.

Mainprice, D., Barruol, G., & Ben Ismail, W., 2000. The seismic anisotropy of the Earth's mantle: from single crystal to polycrystal, in *Earth's Deep Interior: Mineral Physics and Tomography From the Atomic to the Global Scale*, no. 117, pp. 237–264, eds Karato, S., Forte, A. M., Liebermann, R. C., Masters, G., & Stixrude, L., Geophysical Monograph, AGU, Washington D.C.

Rooney, T., Furman, T., Yirgu, G., & Ayalew, D., 2005. Structure of the Ethiopian lithosphere: Xenolith evidence in the Main Ethiopian Rift, *Geochimica et Cosmochimica Acta*, **69**(15), 3889–3910.

Rümpker, G. & Ryberg, T., 2000. New "Fresnel-zone" estimates for shear-wave splitting observations from finite-difference modeling, *Geophys. Res. Lett.*, **27**(13), 2005–2008.

Rümpker, G. & Silver, P. G., 2000. Calculating splitting parameters for plume–type anisotropic structures of the upper mantle, *Geophys. J. Int.*, **143**, 507–520.

Rümpker, G., Ryberg, T., Bock, G., & Desert Seismology Group, 2003. Boundary–layer mantle flow under the Dead Sea transform fault inferred from seismic anisotropy, *Nature*, **425**, 497–501.

Savage, M. K., 1999. Seismic anisotropy and mantle deformation: What have we learned from shear wave splitting?, *Rev. Geophys.*, **37**(1), 65–106.

Silver, P. G., 1996. Seismic anisotropy beneath the continents: Probing the depths of geology, *Annu. Rev. Earth Planet. Sci*, **24**, 385–432.

Silver, P. G. & Chan, W. W. J., 1991. Shear–wave splitting and subcontinental mantle deformation, *J. Geophys. Res.*, **96**, 16429–16454.

Silver, P. G. & Savage, M. K., 1994. The interpretation of shear wave splitting parameters in the presence of two anisotropic layers, *Geophys. J. Int.*, **119**, 949–963.

Stuart, G. W., Bastow, I. D., & Ebinger, C. J., 2006. Crustal structure of the northern Main Ethiopian Rift from receiver function studies, in *The Afar volcanic province within the east African rift system*, no. 259, pp. 55–72, eds Yirgu, G., Ebinger, C. J., & Maguire, P. K. H., Geological Society, Special Publication, London, UK.

Teanby, N. A., Kendall, J.-M., & Van der Baan, M., 2004. Automation of shear–wave splitting measurements using cluster analysis, *Bull. Seis. Soc. Am.*, **94**(2), 453–463.

Whaler, K. A. & Hautot, S., 2006. The electrical resistivity structure of the crust beneath the northern Main Ethiopian Rift, in *The Afar volcanic province within the east African rift system*, no. 259, pp. 55–72, eds Yirgu, G., Ebinger, C. J., & Maguire, P. K. H., Geological Society, Special Publication, London, UK.

Figure 1. Average *SKS*-wave splitting results beneath the Main Ethiopian Rift (MER), adapted from Kendall et al. (2005). The orientation of the white bars shows the fast shear-wave direction, and the length is proportional to the amount of splitting. Heavy black lines indicate major border faults and magmatic segments are marked in red. The solid white line perpendicular to the rift indicates the profile used to construct the top panels. The inset plot shows the location of the EAGLE array in Ethiopia. The top panels show shear-wave splitting parameters as a function of distance from the rift axis. The red triangles show an interpolated fit to the data using a cubic B-spline interpolation with a knot spacing of 30 km. The shaded region shows the r.m.s. misfit of the data from the curve over a 30 km sliding window.

Figure 2. (Top) a schematic representation of the model used in the one-way wave equation modelling scheme. (Bottom) Hemispherical projections of the elastic constants applied at each node. The colour scheme shows the variation of magnitude of shear-wave anisotropy, and the black ticks show the fast direction of a wave propagating through the anisotropic medium, as a function of direction of propagation. Elastic constants are calculated for vertically aligned melt pockets using the approach of Hudson (1981), see text for details. For the modelling the symmetry plane on the rift flanks is oriented 30° from north, and in the rift segment it is oriented north-south. All other parameters (rift width, amount of anisotropy, depth extent of anisotropy, frequency of incoming wave and initial polarisation of incoming wave), are varied systematically (Table 1) and results are displayed in Figures 3-7.

Figure 3. Model 1: Varying rift width. Other parameters: maximum *S*-wave anisotropy=10%, anisotropic depth=45 km, Period=8 s, initial polarisation=45°. Coloured dashed lines indicate the rift width for each model. Note smooth transition in ϕ, with inflexion points marking rift width, and complicated variation of δt.

Figure 4. Model 2: Varying maximum *S*-wave anisotropy. Other parameters: rift width=40 km, anisotropic depth=45 km, Period=8 s, initial polarisation=45°. Black dashed line indicates the rift width for the model. Note similar curves to model 1, but with the δt varying proportionally to the amount of anisotropy. The peaks and troughs in the δt profile do not change with varying amounts of anisotropy.

Figure 5. Model 3: Varying anisotropic depth. Other parameters: rift width=40 km, maximum *S*-wave anisotropy =10%, Period=8 s, initial polarisation=45°. Black dashed line indicates the rift width for the model. Note similar curves to model 2, but now the peaks and troughs in the δt profile moveout with increasing depth of the anisotropic layer. The flexure points still mark out the rift width, except for the 85 km case where multi-pathing effects cause a deviation in the ϕ profile.

Figure 6. Model 4: Varying frequency of incoming wave. Other parameters: rift width=40 km, maximum *S*-wave anisotropy=10%, anisotropic depth=45 km, initial polarisation=45°. Black dashed line indicates the rift width for the model. Note higher frequencies approach a ray based model, and show little deviation from the input model. inflexion points in the ϕ profile still map out the rift width.

Figure 7. Model 5: Varying initial polarisation. Other parameters: rift width=40 km, maximum *S*-wave anisotropy=10%, anisotropic depth=45 km, frequency=8 s. Black dashed line indicates the rift width for the model. Note a high variability in δt and ϕ profiles with initial polarisation.

Figure 8. An example of the Teanby et al. (2004) method of splitting for a) EAGLE station ADEE (Event information: 2001/12/02, 13:01:53, 39.40°N, 141.09°E, 123.8km, MW6.5), after Kendall et al. (2005). b) Synthetic data for an MER model (Figure 9). Both traces are located on the Eastern margin of the rift zone. (i and vii) Traces rotated into R and T directions before and after the anisotropy correction. R component is the initial shear-wave polarisation before entering the anisotropic region. T component is perpendicular to the R component. Energy on the corrected transverse trace should be minimised in the analysis window. (ii and viii) Uncorrected fast/slow shear waveforms. (iii and ix) Corrected fast/slow shear waveforms. (iv and x) Particle motion for uncorrected seismograms. (v and xi) Particle motion for corrected seismograms. A good result will show similar fast/slow waveforms and any elliptical particle motion will be linearised. (vi and xii) The results of the grid search over δt and ϕ. The method used minimises the second eigenvalue of the particle motion (i.e. the best result occurs where the particle motion is linear after removing the splitting). The optimum splitting parameters are represented by the cross, and the 1st surrounding contour denotes the 95% confidence interval.

Figure 9. Best fitting model to the results of Kendall et al. (2005). Rift width=100 km, maximum *S*-wave anisotropy=9%<-14 km, anisotropy=7%>-14 km, anisotropic depth=90 km, frequency=8 s, initial polarisation=40°. The δt model results are compared to splitting results from one event with a back azimuth of 40°, and the ϕ model results are compared with all splitting results.

Figure 10. (Top) variation in δt profile with varying depth extent of anisotropy (similar to model 3). Blue dashed line shows the moveout with depth of the peaks in the δt profile. (Bottom) Least-squares fit to the location of the peaks in the δt profile with depth. Model parameters used in this model are rift width=100 km, maximum *S*-wave anisotropy=10%, variable anisotropic depth, frequency=8 s, initial polarisation=40°.

Figure 11. Map (left) and cross-section (right) view of the best fitting model from Figure 9, plotted over the *P*-wave tomographic images of Bastow et al. (2008). The red lines on the left plot highlight the modelled rift edges, and the dashed black line indicates the transition from 9% anisotropy to 7%. The white lines indicate the location of the tomographic cross-sections. There is a strong correlation between the slow velocity anomalies and the regions of 9% anisotropy. Also the slowest anomalies appear to be present in the top 100km, similar to where we constrain the anisotropy to be.

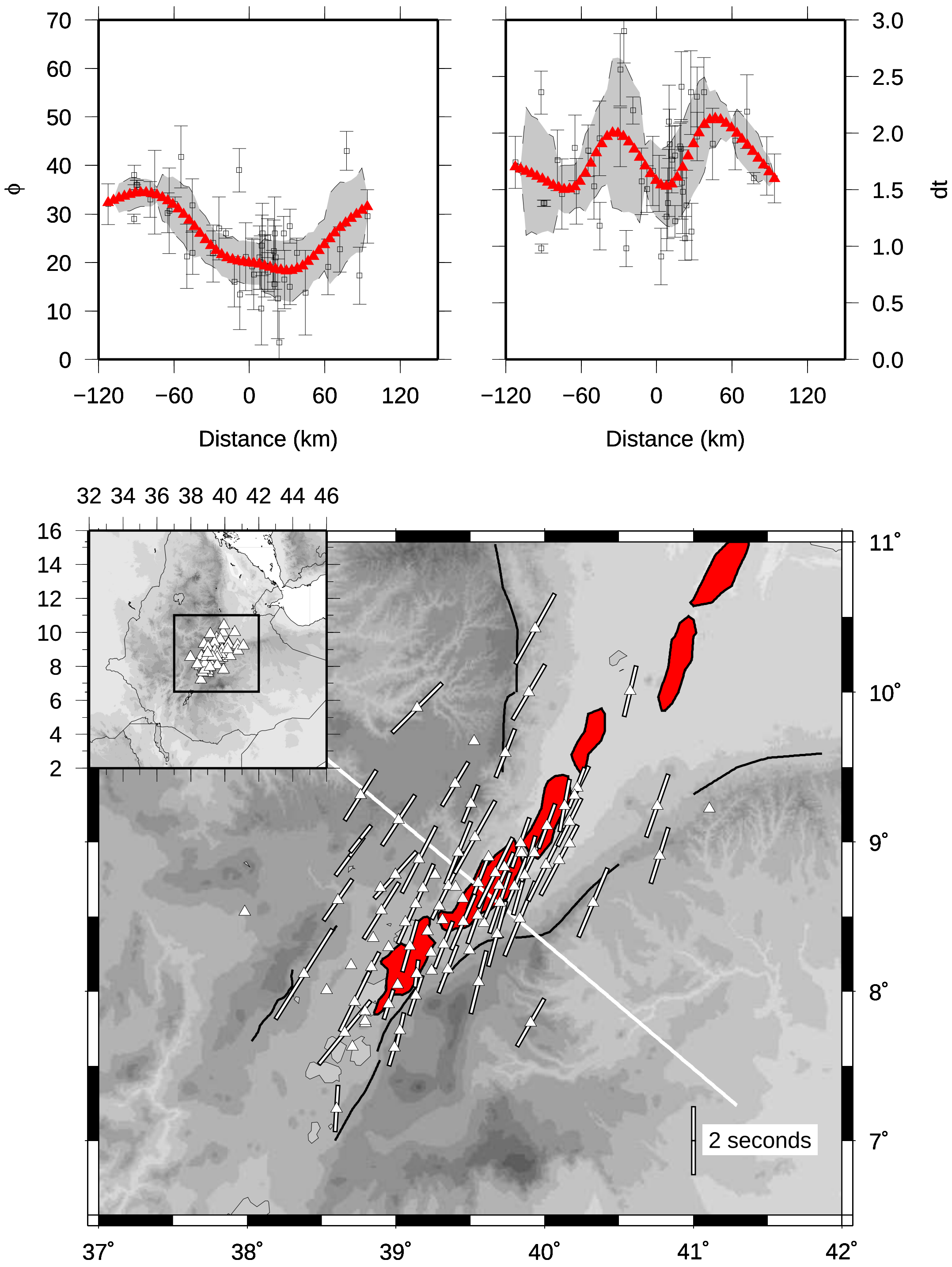

Figure 1

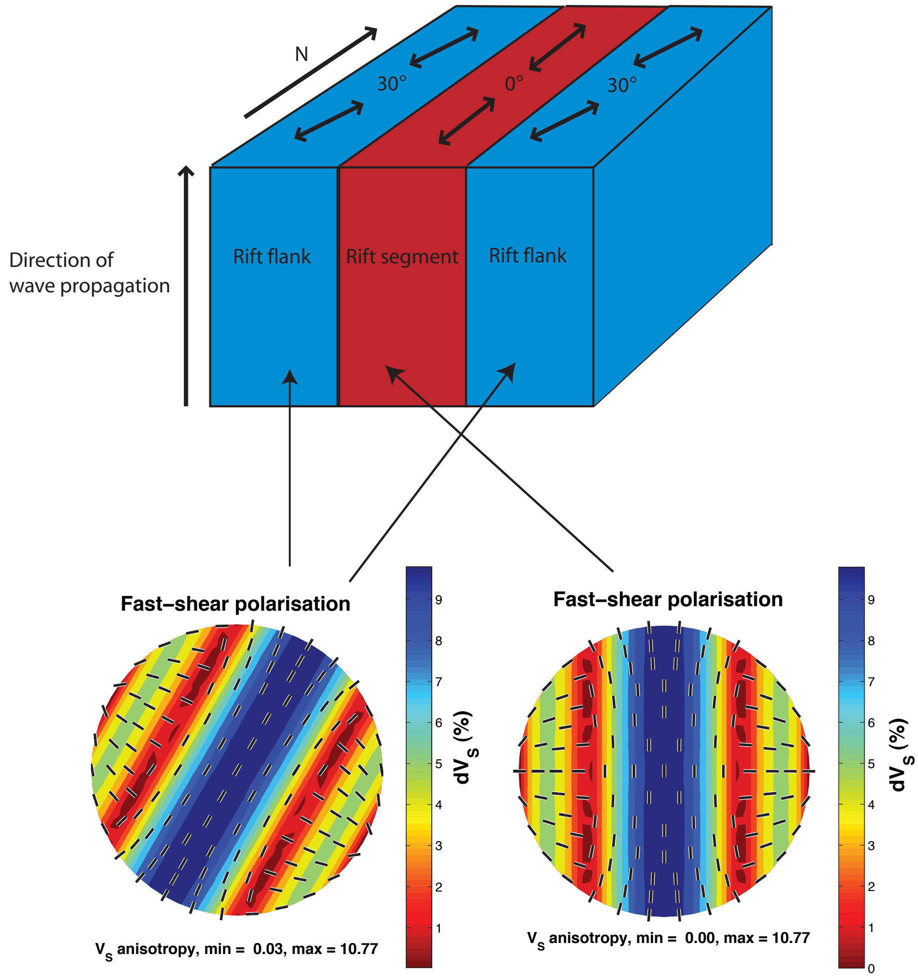
N
30°
0°
30°
Direction of
wave propagation
Rift flank
Rift segment
Rift flank
Fast–shear polarisation
V_S anisotropy, min = 0.03, max = 10.77
Fast–shear polarisation
V_S anisotropy, min = 0.00, max = 10.77
dV$_S$ (%)
dV$_S$ (%)

Figure 2

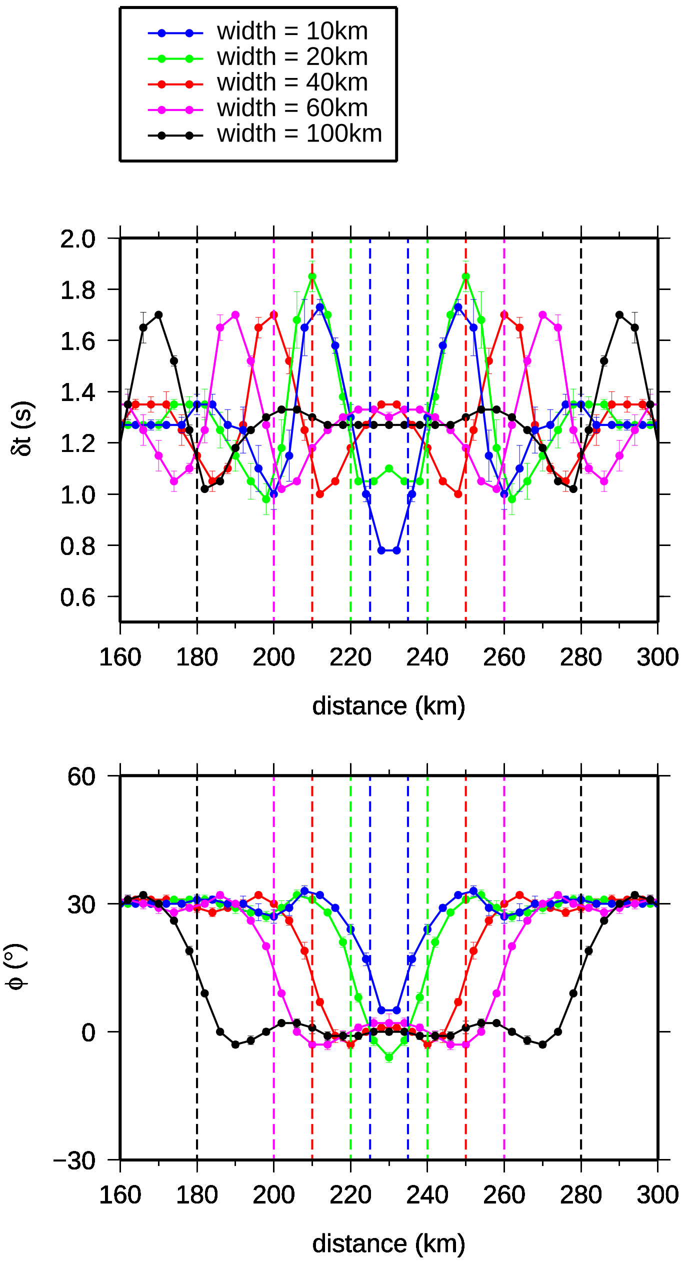
width = 10km
width = 20km
width = 40km
width = 60km
width = 100km
δt (s)
2.0
1.8
1.6
1.4
1.2
1.0
0.8
0.6
160
180
200
220
240
260
280
300
distance (km)
60
30
0
−30
φ (°)
160
180
200
220
240
260
280
300
distance (km)

Figure 3

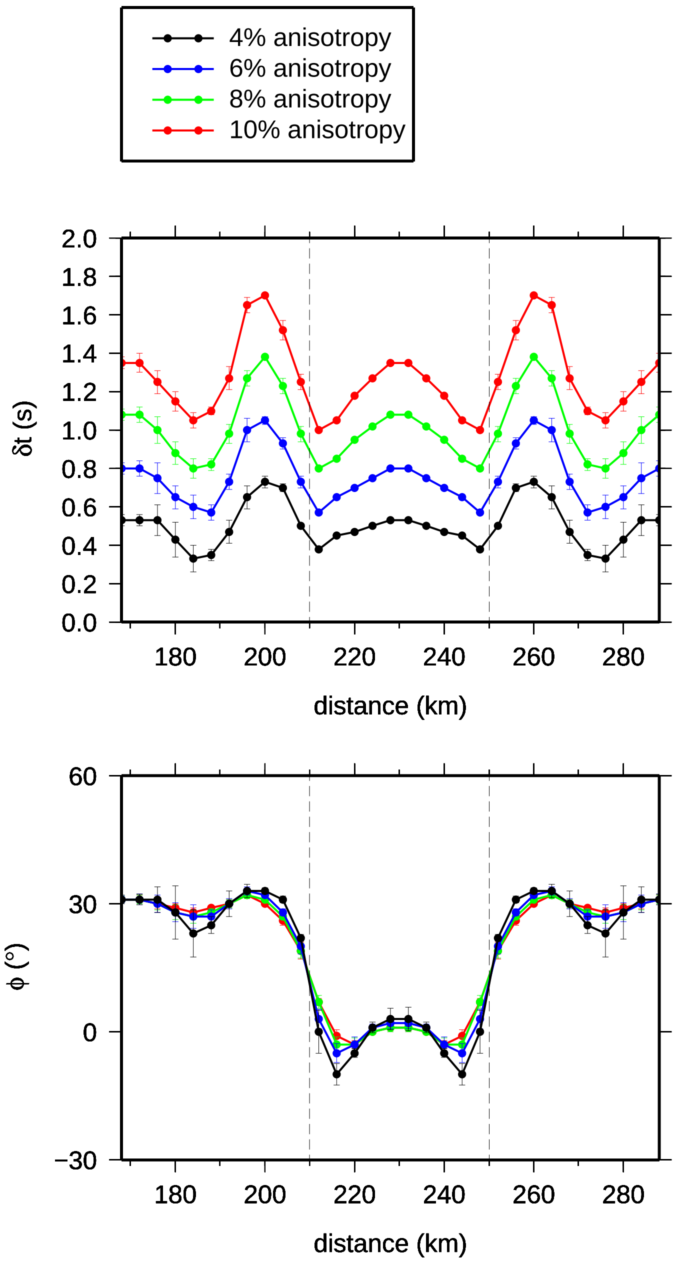
4% anisotropy
6% anisotropy
8% anisotropy
10% anisotropy
2.0
1.8
1.6
1.4
1.2
1.0
0.8
0.6
0.4
0.2
0.0
δt (s)
180
200
220
240
260
280
distance (km)
60
30
0
−30
φ (°)
180
200
220
240
260
280
distance (km)

Figure 4

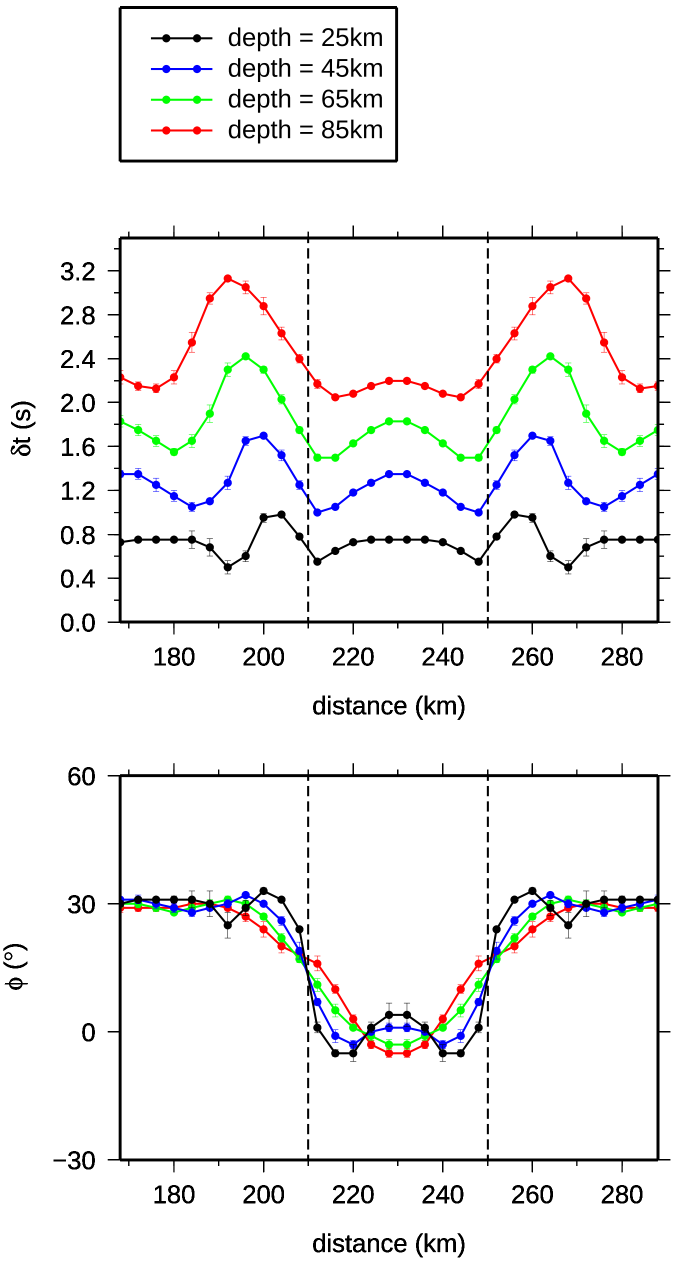
depth = 25km
depth = 45km
depth = 65km
depth = 85km
δt (s)
3.2
2.8
2.4
2.0
1.6
1.2
0.8
0.4
0.0
180
200
220
240
260
280
distance (km)
ϕ (°)
60
30
0
−30
180
200
220
240
260
280
distance (km)

Figure 5

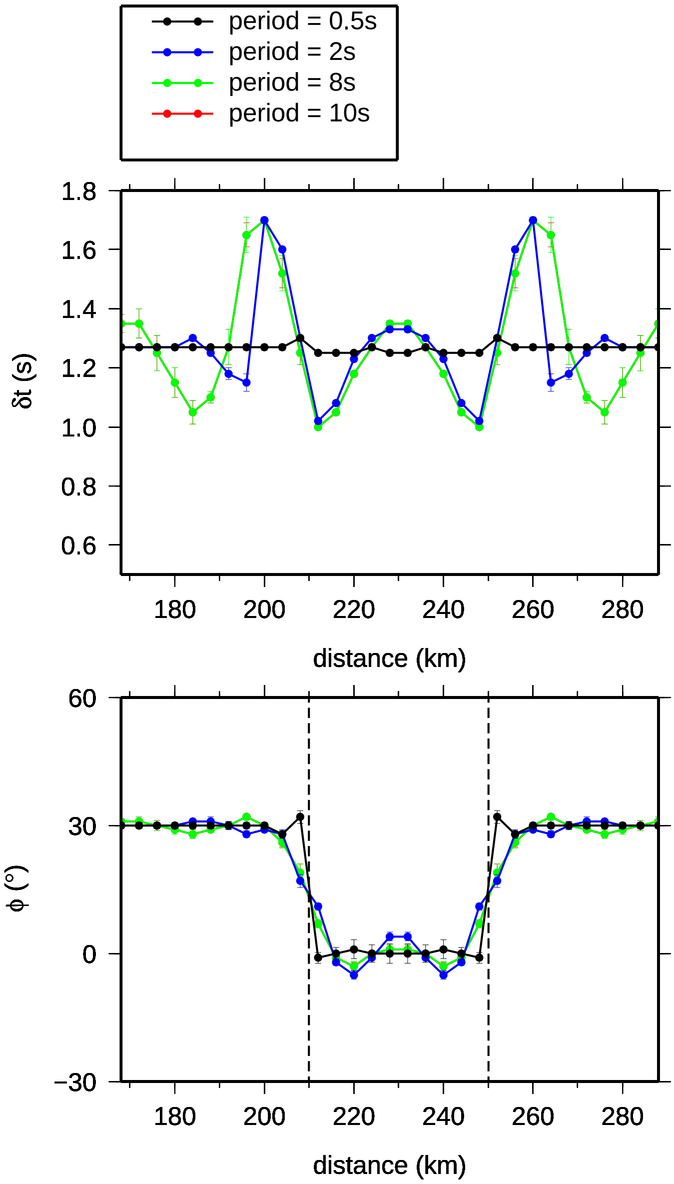
period = 0.5s
period = 2s
period = 8s
period = 10s
1.8
1.6
1.4
1.2
1.0
0.8
0.6
δt (s)
180
200
220
240
260
280
distance (km)
60
30
0
−30
φ (°)
180
200
220
240
260
280
distance (km)

Figure 6

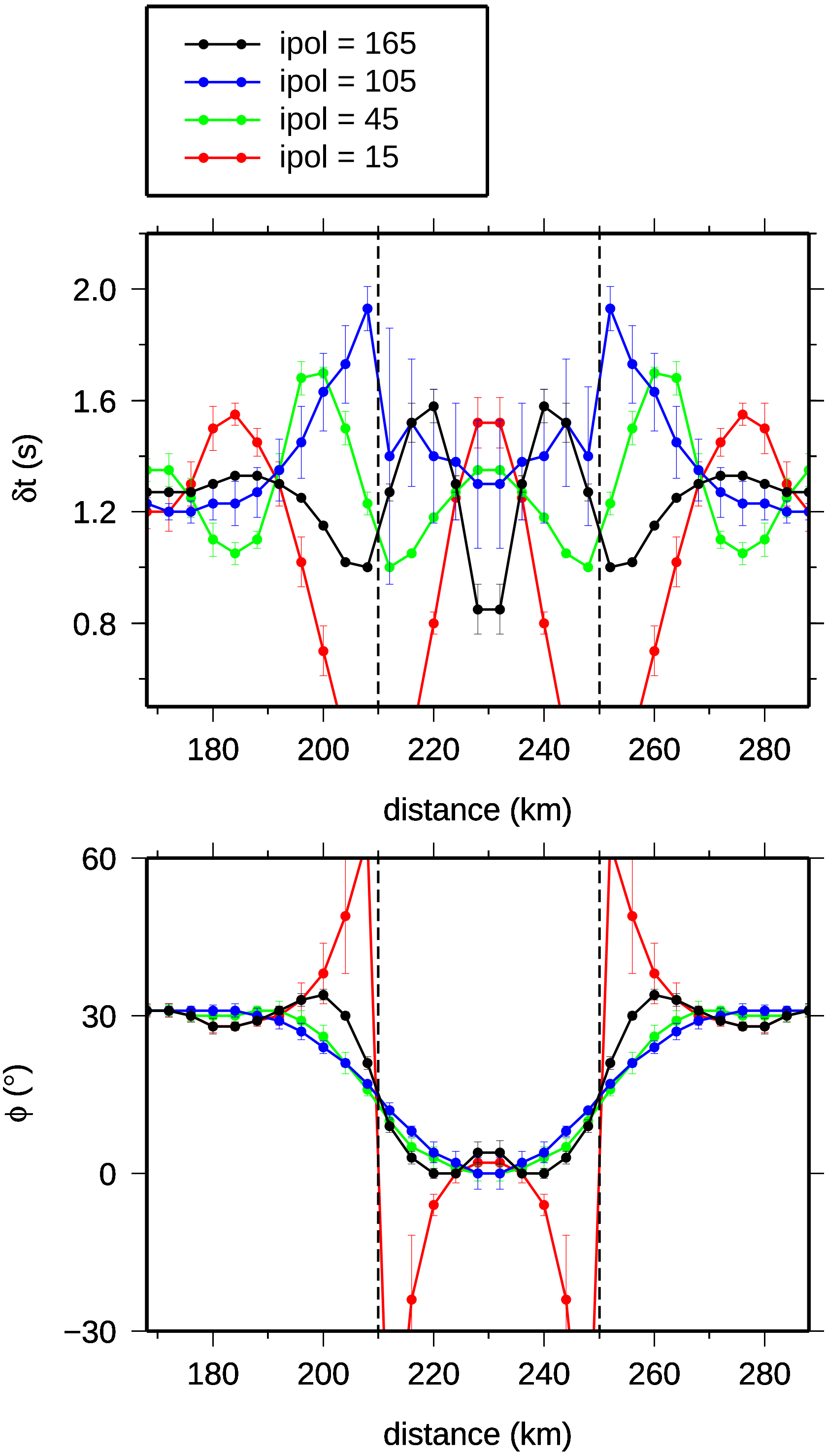
ipol = 165
ipol = 105
ipol = 45
ipol = 15
δt (s)
2.0
1.6
1.2
0.8
180
200
220
240
260
280
distance (km)
ϕ (°)
60
30
0
−30
180
200
220
240
260
280
distance (km)

Figure 7

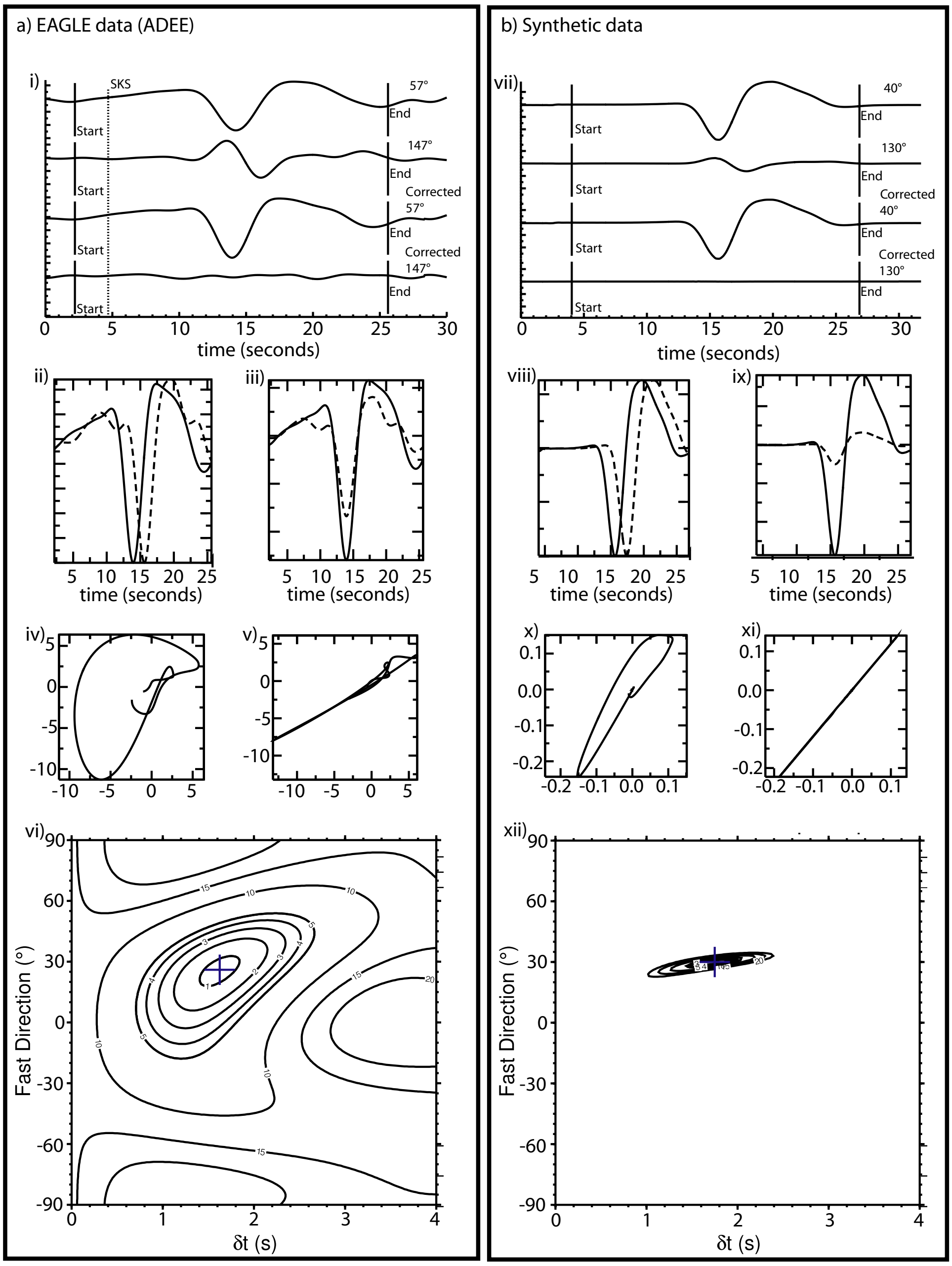
a) EAGLE data (ADEE)
b) Synthetic data
i)
SKS
57°
147°
Corrected 57°
Corrected 147°
Start
End
time (seconds)
ii)
iii)
iv)
v)
vi)
Fast Direction (°)
δt (s)
vii)
40°
130°
Corrected 40°
Corrected 130°
viii)
ix)
x)
xi)
xii)

Figure 8

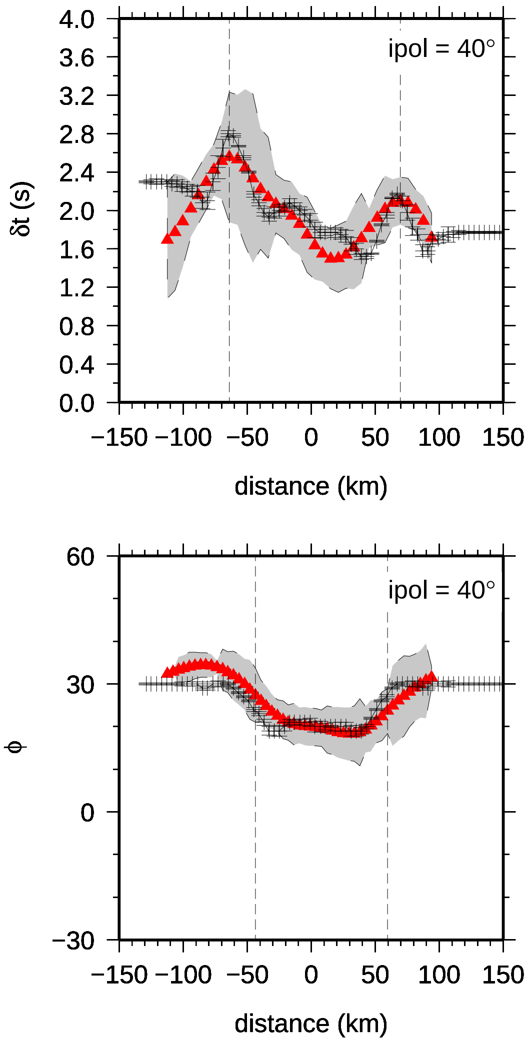
4.0
3.6
3.2
2.8
2.4
2.0
1.6
1.2
0.8
0.4
0.0
δt (s)
ipol = 40°
−150 −100 −50 0 50 100 150
distance (km)
60
30
0
−30
φ
ipol = 40°
−150 −100 −50 0 50 100 150
distance (km)

Figure 9

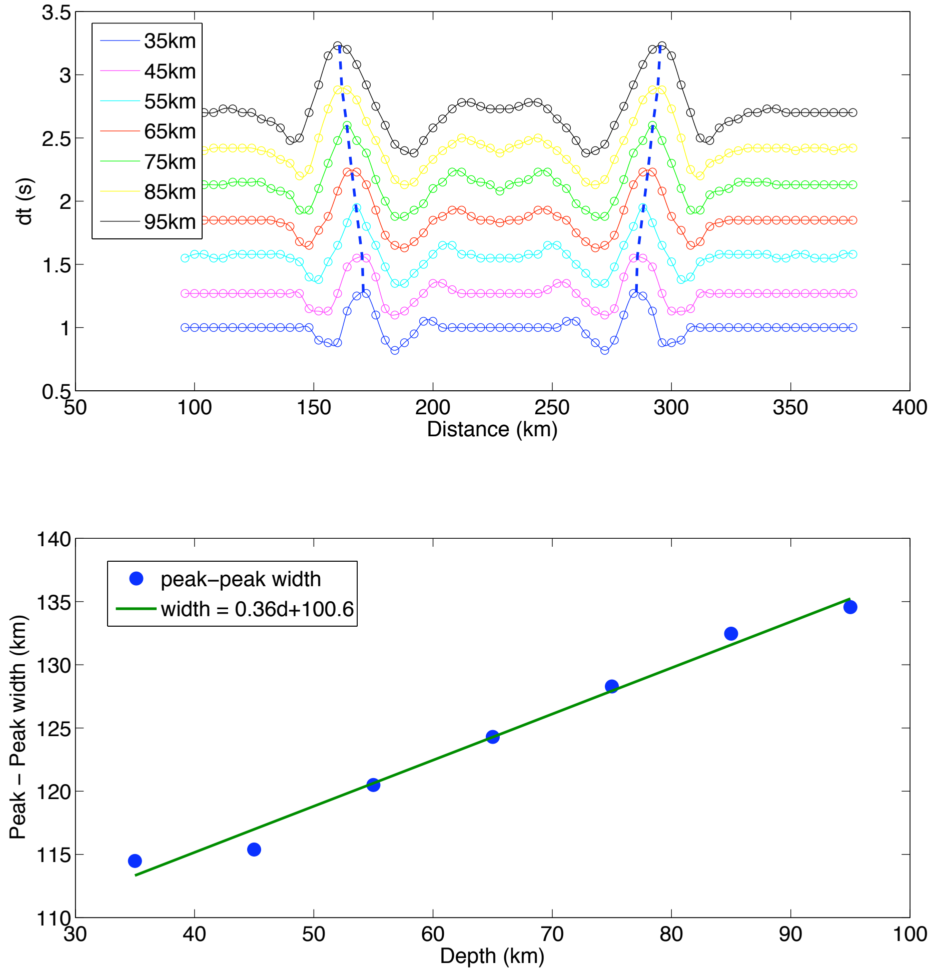
35km
45km
55km
65km
75km
85km
95km
dt (s)
Distance (km)
peak–peak width
width = 0.36d+100.6
Peak – Peak width (km)
Depth (km)

Figure 10

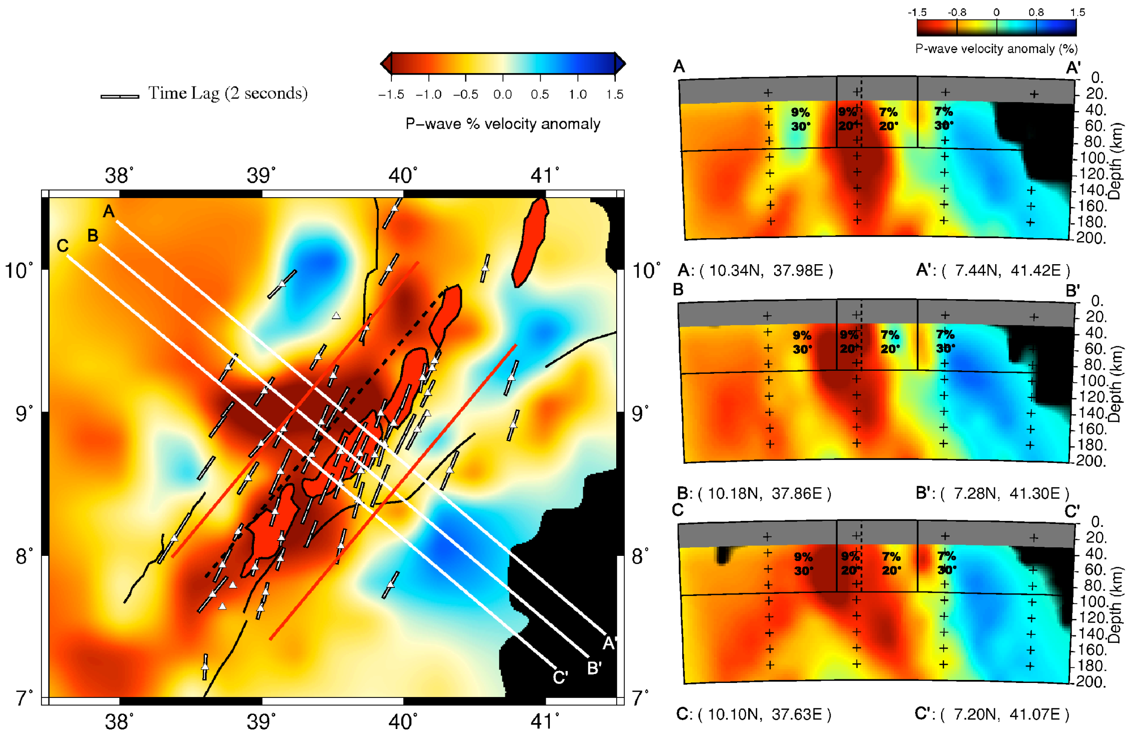
Time Lag (2 seconds)
P–wave % velocity anomaly
P-wave velocity anomaly (%)
A: (10.34N, 37.98E)
A': (7.44N, 41.42E)
B: (10.18N, 37.86E)
B': (7.28N, 41.30E)
C: (10.10N, 37.63E)
C': (7.20N, 41.07E)
Depth (km)

Figure 11